Meso-Beta Scale Numerical Simulation Studies of Terrain-Induced Jet Streak Mass/Momentum Perturbations

FY94 May Semi-Annual Report

submitted to the
Mesoscale Processes Research Program
Atmospheric Dynamics and Radiation Branch
Earth Science and Application Division
Office of Space Science and Applications
NASA Headquarters
Washington, D. C. 20546
Attention: Dr. Ramish Kakar, Program Manager

by

Yuh-Lang Lin and Michael L. Kaplan
Department of Marine, Earth, and Atmospheric Sciences
North Carolina State University
Raleigh, North Carolina 27695-8208
(919) 515-7977

May 1994

Table of Contents

Part I. 3D Numerical Modeling Studies of Terrain-Induced Mass/Momentum Perturbations

1. Introduction

Recently, Koch and Dorian (1988) produced an in-depth analysis of observed gravity waves and their relationship to precipitation bands over the Montana mesonetwork during the 11-12 July 1981 CCOPE case study. Their analyses indicated two episodes of coherent waves. One of the fundamental unanswered questions from this research, however, concerns the dynamical processes which generated the waves, all of which originated from the region encompassing the borders of Montana, Idaho, and Wyoming. While geostrophic adjustment, shearing instability, and terrain where all implicated separately or in concert as possible wave generation mechanisms, the lack of upper-air data within the wave genesis region (WGR, Fig. 1) made it difficult to rigorously define the genesis processes from observations alone. In this paper we will employ a mesoscale numerical model to help us diagnose the intricate *early* wave generation mechanisms during the first observed gravity wave episode.

2. Synoptic-Scale Observations

At 0000 UTC 11 July 1981 a massive ridge of high pressure covered most of the western Great Plains and intermountain region of the U. S. and southwestern Canada, while a cutoff low was located over coastal Washington (not shown). In between, the polar jet streak stretched from northern California to southwestern Saskatchewan with its right exit region being located over western Montana. The inflection point in the ridge was in proximity to the right exit region of the jet streak. Also evident from individual wind component analyses and satellite imagery (not shown) is the development of a secondary jet streak structure some 200-300 km to the southeast of the primary jet during the 0000 UTC - 1200 UTC period. In addition, a weak short wave trough is observed to

intensify over western Montana by 1200 UTC as it propagates northeastward and the low-level wind flow accelerates towards the north over the WGR at the same time.

3. Numerical Experiments

The hydrostatic numerical model employed for the simulation experiments is the Goddard version of the MASS model (e.g. Manobianco *et al.* 1994). A matrix of 223 x 146 x 30 grid points was centered over the northern Rocky Mountain region with ~16 km horizontal resolution, while an identical nested grid matrix was centered over west-central Montana with ~8 km horizontal resolution. The coarse mesh simulation was initialized at 0000 UTC 11 July 1981 from standard LFM analysis data, rawinsondes, and surface observations and integrated through 0600 UTC 12 July 1981. The nested-grid simulation was initialized at 0900 UTC 11 July 1981 and integrated through 0600 UTC 12 July 1981. Initial and boundary conditions for the nested-grid simulation were derived from the coarse mesh simulation. While several physics and terrain sensitivity experiments have been performed, for brevity we will only compare a coarse mesh constant terrain elevation simulation with no latent heating (A) and a nested-grid high resolution terrain simulation with no latent heating (B) to diagnose the geostrophic adjustment processes which contribute to the organization of gravity wave episode #1 which develops shortly after 1200 UTC 11 July.

4. Primary Geostrophic Adjustment Period

Figure 1 depicts the simulation A sequence of 500 mb wind vectors and isotachs during the 0000 UTC - 0600 UTC time period. Evident is a dramatic modification of the jet streak exit region structure as the velocity maximum over west central Idaho at 0000 UTC encounters the changing pressure gradient force over western Montana. By 0300 UTC (not shown) a secondary velocity maximum (J_2 in Fig. 1b) develops to the north of the 0000 UTC maximum. This secondary maximum is the result of the increased cross-

stream-directed pressure gradient force encountered by parcels exiting the jet streak over western Montana. This results in a local increase of the cross-stream wind velocity component. Three hours later the inertial-advective terms in the equations of motion adjust to the northward acceleration by increasing the along-stream wind component to the southeast of the secondary maximum. Thus, the rotational wind increases downstream over central Montana so that by 0600 UTC a new southeastward-shifted "jetlet" (J3) has formed, thus bifurcating the original jet structure. Therefore, the wind has geostrophically adjusted to the mass field forming a split jet streak structure just northwest of the WGR. This is consistent with satellite imagery showing a secondary cirrus plume over southeastern Idaho at 0600 UTC which redevelops northeastward to southwestern Montana by 0900 UTC (not shown).

5. Geostrophic Adjustment Frontogenesis

Consistent with the aforementioned adjustment process in simulation A is the development of a thermally-indirect circulation oriented *both across and along* the stream. This circulation is in response to the velocity divergence and convergence patterns accompanying the secondary "jetlet" formation northwest of the WGR. The mass field adjusts to the secondary jetlet by inducing midtropospheric ascent on the cyclonic and upstream side and midtropospheric descent on the anticyclonic and downstream side resulting in adiabatic cooling and warming patterns by 0500 UTC and frontogenesis northwest of the WGR during the 0200 UTC - 0800 UTC period (note Figure 2).

6. Secondary Geostrophic Adjustment

The jetlet which induces the aforementioned frontogentical circulation propagates downstream over Montana during the 0800 UTC through 1200 UTC period. At this time

the new midtropospheric mass perturbation coupled to the aforementioned midtropospheric front induces a secondary geostrophic adjustment process to the south and east of the primary geostrophic adjustment region, i. e., near the WGR. By 1300 UTC the simulation A 500 mb winds and vertical motions (Figure 3) indicate that this secondary jetlet's exit region has produced an along-stream thermally-indirect circulation along the southeastern periphery of the previous jetlet's circulation, thus resulting in ascent, saturation, and velocity divergence directly over the WGR at the time of the initial gravity wave generation. The flow in this region at this time is *highly ageostrophic and unbalanced.* Beneath the midtropospheric circulation can be seen the exit region of a newly-formed 700 mb low-level jet (LLJ) which has been induced by the enhanced height falls just upstream from the WGR under the secondary midtropospheric jetlet and in proximity to the propagating low-level short wave trough. A "bulls eye" pattern of relative humidity near the WGR (not shown) forced by the convergence accompanying the LLJ is consistent with the development of convection and the first gravity wave episode which are both observed to commence at approximately 1300 UTC.

7. Genesis of Gravity Waves

Figure 4 depicts the generation of internal gravity waves by simulation B. These features, evident in the 500 mb vertical velocity field have a wavelength consistent with the primary modes observed by Koch and Dorian (1988), however, they produce a weaker pressure signal and move somewhat slower. These waves are virtually absent in the coarse mesh simulations yet are somewhat stronger as the terrain resolution is enhanced. At this stage of the analysis of the various simulations it is evident that geostrophic adjustment initiates internal gravity waves, however, their amplification appears to be affected by: (i) terrain-induced adiabatic ascent and descent, (ii) latent heating, and (iii) differential surface sensible heat flux.

8. Summary and Conclusions

The role of multiple geostrophic adjustment processes in focusing a region for gravity wave genesis has been studied with various simulations from a meso-beta scale numerical model. The focusing of wave genesis near in space and time to where it is observed is the result of the following sequence of processes: 1) a cross-stream acceleration of the wind field is followed by an along-stream acceleration within the exit region of a jet streak which encounters the inflection point in the height field, 2) the resulting wind pattern represents the bifurcation of the jet streak into multiple maxima displaced to the southeast of the original maximum but still northwest of the WGR, 3) the resulting velocity divergence induces differential patterns of ascent and descent both across and along the stream resulting in midtropospheric frontogenesis, 4) a second geostrophic adjustment occurs further southeast of the front which was near the WGR, 5) the vertically integrated divergence produced by the second adjustment over the WGR modifies the mass pattern which induces low-level jet formation, and 6) relatively weak-amplitude gravity waves radiate downstream towards the CCOPE mesonet region in eastern Montana.

Part II. Linear Theory and Theoretical Modeling

1. Introduction

The response of non-resting rotating homogeneous and continuously stratified Boussinesq models of the terrestrial atmosphere to temporally impulsive and uniformly propagating three-dimensional localized zonal momentum sources representative of midlatitude jet streaks is investigated. The methods of linear perturbation theory applied to the potential vorticity (PV) and wave field equations are used to study the geostrophic adjustment dynamics associated with the initial value problem imposed by the introduction of an ageostrophic zonal jet in a uniform geostrophically balanced barotropic

flow, as well as the forced problem imposed by an external momentum forcing traveling at the speed $c < U$ within the basic state current. Effects of nonlinearity are investigated using simple numerical shallow water and continuously stratified primitive equation models. The total zonal and meridional wind perturbations are separated into geostrophic and ageostrophic components in order to define and follow the evolution of both the primary and secondary mesocirculations accompanying midlatitude jetogenesis forced by geostrophic adjustment processes.

This problem is addressed in order to help fill the gap in our understanding of the dynamics and structure of mesoscale inertia-gravity waves forced by geostrophic adjustment processes in simple two-dimensional quiescent current systems (Rossby, 1938; Cahn, 1945) and those produced by mesoscale numerical models simulating the orographic and diabatic perturbation of three-dimensional quasi-geostrophically balanced synoptic scale jet streaks associated with complex baroclinic severe storm producing environments (Kaplan *et al.*, 1994a, b).

For brevity only the theory governing and figures illustrating features of the small-amplitude response in a rotating Boussinesq atmosphere are presented here. Details concerning the response in a homogeneous atmosphere of finite depth as well as a more rigorous discussion of the continuously stratified response in both infinite and semi-infinite Boussinesq atmospheres can be found in Weglarz (1994).

2. Theory

The field equations governing small-amplitude baroclinic perturbations in a rotating Boussinesq atmosphere forced by zonal (F_x) and meridional (F_y) momentum sources, diabatic heating/cooling (Q), and shallow orography may be combined to yield the linearized potential vorticity and wave field equations, which are written collectively as

$$L\,\phi'(x,y,z,t) = S(x,y,z,t) \ , \qquad (1)$$

where $\phi' = q'$, $\mathbf{u} = (u', v', w')$, p' or θ'; $q' = \zeta' + (f/\rho_o N^2)\partial^2 p'/\partial z^2$ is the linearized PV, and where the differential operators L and inhomogeneous source terms $S(\mathbf{r},t)$ are defined as

$$L = \begin{cases} \dfrac{\partial}{\partial t} + U\dfrac{\partial}{\partial x} + V\dfrac{\partial}{\partial y}, & \text{if } \phi' = q' \\ [(\dfrac{\partial}{\partial t} + U\dfrac{\partial}{\partial x} + V\dfrac{\partial}{\partial y})^2 + f^2]\dfrac{\partial^2}{\partial z^2} + N^2\nabla_H^2, & \text{if } \phi' = \mathbf{u}', p', \theta' \end{cases} \tag{2}$$

$$S(\mathbf{r},t) = \begin{cases} F\zeta + \dfrac{f\,g}{N^2 c_p T_0}\dfrac{\partial Q}{\partial z}, & \text{if } \phi' = q' \\ -N^2\dfrac{\partial q'}{\partial y} + \dfrac{\partial^2}{\partial z^2}(\dfrac{DF_x}{Dt} + f F_y) - \dfrac{g}{c_p T_0}\dfrac{\partial^2 Q}{\partial z \partial x}, & \text{if } \phi' = u' \\ N^2\dfrac{\partial q'}{\partial x} + \dfrac{\partial^2}{\partial z^2}(\dfrac{DF_y}{Dt} - f F_x) - \dfrac{g}{c_p T_0}\dfrac{\partial^2 Q}{\partial z \partial y}, & \text{if } \phi' = v' \\ -\dfrac{\partial}{\partial z}(\dfrac{DF_\delta}{Dt} + f F\zeta) + \dfrac{g}{c_p T_0}\nabla_H^2 Q, & \text{if } \phi' = w' \\ \rho_0[N^2(f q' + F_\delta) + \dfrac{g}{c_p T_0}\dfrac{D}{Dt}\dfrac{\partial Q}{\partial z}], & \text{if } \phi' = p' \\ \dfrac{\theta_0}{g}\dfrac{\partial}{\partial z}(\rho_0[N^2(f q' + F_\delta) + \dfrac{g}{c_p T_0}\dfrac{D}{Dt}\dfrac{\partial Q}{\partial z}]), & \text{if } \phi' = \theta' \end{cases} \tag{3}$$

where $F\zeta = \mathbf{k}\cdot\nabla\times\mathbf{F}$, $F_\delta = \nabla\cdot\mathbf{F}$, $\nabla^2_H = \partial^2/\partial x^2 + \partial^2/\partial y^2$ is the two-dimensional horizontal Laplacian, and the other symbols carry their conventional meteorological and mathematical meanings.

2.1 *Method of Solution*

The Fourier transform of any dynamical field variable and its inverse in a vertically unbounded Boussinesq atmosphere may be defined by the integral pair

$$\widehat{\phi}(\mathbf{k},t) = \frac{1}{(2\pi)^3} \int_{-\infty}^{\infty} \int_{-\infty}^{\infty} \int_{-\infty}^{\infty} \phi'(\mathbf{r},t)\, e^{-i\,\mathbf{k}\cdot\mathbf{r}}\, d\mathbf{r}\,, \tag{4}$$

$$\phi'(\mathbf{r},t) = \int_{-\infty}^{\infty} \int_{-\infty}^{\infty} \int_{-\infty}^{\infty} \widehat{\phi}(\mathbf{k},t)\, e^{+i\,\mathbf{k}\cdot\mathbf{r}}\, d\mathbf{k}\,, \tag{5}$$

where $\mathbf{r} = (x,y,z)$, and $\mathbf{k} = (k,l,m)$. The Fourier transform of the linearized PV and wave field equations in the absence of diabatic and orographic forcing yield

$$\frac{\partial \widehat{q}}{\partial t} + i\,\Omega\,\widehat{q} = -\,i\,l\,\widehat{F}_{\xi}, \tag{6}$$

$$\frac{\partial^2 \widehat{\phi}}{\partial t^2} + 2\,i\,\Omega\,\frac{\partial \widehat{\phi}}{\partial t} + R(\mathbf{k})\widehat{\phi} = \widehat{S}_{\xi}(\mathbf{k},t)\,, \tag{7}$$

where

$$R(\mathbf{k}) = f^2 + \frac{N^2}{m^2}\kappa^2 - \Omega^2, \tag{8}$$

and the inhomogeneous source terms are given by

$$\hat{S}_\xi(\mathbf{k},t) = \begin{Bmatrix} i\,(l\frac{N^2}{m^2}\hat{q} + \Omega\hat{F}_\xi), & \text{if } \hat{\phi} = \hat{u} \\ -i\,k\frac{N^2}{m^2}\hat{q} - f\hat{F}_\xi, & \text{if } \hat{\phi} = \hat{v} \\ [\frac{(l\,f - i\,k\,\Omega)}{m}]\,\hat{F}_\xi, & \text{if } \hat{\phi} = \hat{w} \\ -\rho_0\frac{N^2}{m^2}(f\hat{q} + i\,k\,\hat{F}_\xi), & \text{if } \hat{\phi} = \hat{p} \\ -i\,\theta_0\frac{N^2}{m\,g}(f\hat{q} + i\,k\,\hat{F}_\xi), & \text{if } \hat{\phi} = \hat{\theta} \end{Bmatrix}. \tag{9}$$

$\Omega = k(U\text{-}c) + lV$ is the relative wave frequency and F_ξ is the vorticity of the external momentum forcing in a frame of reference translating at the zonal speed c through the basic state flow. Note that in this frame the applied forcing is *stationary*. The general solutions are found to be

$$\hat{q}(\mathbf{k},t) = [\hat{q}_i(\mathbf{k}) + \frac{1}{\Omega}\hat{F}_\xi(\mathbf{k})]\,e^{-i\,\Omega\,t} - \frac{1}{\Omega}\hat{F}_\xi(\mathbf{k}), \tag{10}$$

$$\hat{\phi} = A_\phi e^{+i\,\omega_-\,t} + B_\phi e^{-i\,\omega_+\,t} + C_\phi e^{-i\,\Omega\,t} + D_\phi\ . \tag{11}$$

The coefficients A_ϕ, B_ϕ, C_ϕ, and D_ϕ are determined by applying appropriate initial conditions to the initial value and forced geostrophic adjustment problems, respectively. Details can be found in Weglarz (1994). The frequencies of the transient dispersive inertia-gravity waves represented by the first two terms on the r.h.s. of Eq. (11) are given by

$$\omega_\pm = \sqrt{f^2 + \frac{N^2\kappa^2}{m^2}} \pm \Omega \tag{12}$$

3. Results

Fig. 5 shows the linear response at t = 6 h after the introduction of an ageostrophic zonal wind anomaly whose horizontal and vertical structure is specified to be:

$$u'_i = u'_{jet} = u_{jo} \left(\frac{x^2}{a^2} + \frac{y^2}{b^2} + 1\right)^{-3/2} e^{-z^2/d^2}. \quad (13)$$

The zonal and meridional half-widths a, b are equal and taken to be 50 km, while the vertical e-folding half-depth d is taken to be 2.5 km. The magnitude of the unbalanced zonal jet u_{jo} is specified to be 20 ms^{-1}. The significant radius of deformation is defined by $L_R = N(2d)/f = 500$ km ($N = 10^{-2}$ s^{-1}, $f = 10^{-4}$ s^{-1}). Since $a = b = L_R/10 << L_R$, then the thermodynamic fields will tend to adjust to the rotational part of the initial wind field (Rossby, 1938; Cahn, 1945).

Horizontal cross sections of $\mathbf{u}' = (u', v', w')$ (Figs. 5a, b, and c) and p' (Fig. 5d) are shown at z = 0, the level at which the initial zonal wind anomaly is a maximum (Eq. 13). At this time, outwardly propagating inertia-gravity waves in both the perturbation wind and pressure fields are associated with the non-zero divergence tendency ($\partial\delta'/\partial t$) induced by the ageostrophic zonal jet. The magnitude of the initial jet has fallen to approximately 7.3 ms^{-1} from its initial value of 20 ms^{-1} (Fig. 5a), a reduction of just over 63%. Zonal counter currents ($u' < 0$) of magnitude ~ 2 ms^{-1} exist north (south) of the main jet core, which may be viewed as portions of perturbation return flow around the centers of low (high) pressure becoming established in these regions (Fig. 5d) as the thermodynamic fields (p' and θ') adjust to the nondivergent portion of the perturbation winds. The horizontal structure of θ' is similar to p', and the vertical structures are related hydrostatically ($1/\rho_o \partial p'/\partial z = g\theta'/\theta_o$). At this time transient inertia-gravity waves are also evident in the evolving geostrophic winds (not shown), and are associated with the zonal ($v'_g = 1/(\rho_o f)\partial p'/\partial x$) and meridional ($u'_g = -1/(\rho_o f)\partial p'/\partial y$) gradients of the evolving perturbation pressure field (Fig. 5d).

Within the context of linear theory, no contribution from the initial PV anomaly $q'_i = -\partial u_{jet}/\partial y$ is partitioned to the vertical velocity field, whose response consists totally of transient dispersive inertia-gravity waves (Fig. 5c) yielding, in the balanced equilibrium state, a field of absolutely no vertical motion (not shown). The steady-state

response which conserves PV is a nondivergent geostrophic zonal jet with confluent (diffluent) flow in its entrance (exit) region, supported by a dipole pressure couplet, with centers of cold (warm) air colocated with the center of low (high) pressure at all levels below the level of maximum zonal wind. Centers of warm (cold) air are colocated with the perturbation low (high) pressure centers north (south) of the jet core at all levels above the level of maximum zonal wind. The absolute magnitudes of the steady-state u', v', p', and θ' fields are 9.32 ms^{-1}, 2.2 ms^{-1}, 0.27 mb, and 0.098 K, respectively. This steady-state equilibrium defines a *thermal wind balance* among the baroclinic perturbations throughout the depth of the unbounded Boussinesq atmosphere.

Fig. 6 shows the results seen by a Galilean observer traveling at the speed $c < U$ at t = 12 h after a traveling zonal momentum forcing whose horizontal and vertical structure given by

$$F_x = U^* \frac{\partial}{\partial x} [u_{jo} \{\frac{(x-ct)^2}{a^2} + \frac{y^2}{b^2} + 1\}^{-3/2}] e^{-z^2/d^2} \qquad (14)$$

is introduced into the basic state flow. This applied forcing is chosen to represent the effect of the inertial-advective acceleration the barotropic current (which is itself taken to be representative of the midlatitude jet stream) experiences as it passes through the slower moving quasi-steady jet streak. The zonal and meridional half-widths a and b are equal to 500 km, the e-folding half-depth d = 12.5 km, u_{jo} = 30 ms^{-1}, and $U^* = U-c$, where U = 20 ms^{-1} and c = 10 ms^{-1}. The significant radius of deformation for this case is $L_R = N(2d)/f$ = 2500 km, which is comparable to that of a homogeneous atmosphere of finite depth whose surface temperature is approximately 273 K. Since $a = b = L_R/5 << L_R$, we can expect the thermodynamic fields to adjust to the externally forced wind fields.

At this time the zonal wind field has a structure resembling that of the applied forcing of absolute magnitude ~ 5ms^{-1} due to the imposed initial condition $\partial u'_j/\partial t = F_\xi$ (Fig. 6a). The meridional wind field is dominated by localized southerly (northerly) flow of comparable magnitude north (south) of the forcing center (Fig. 6b), and can be

attributed to the horizontal gradient of the evolving p' field at this level (Fig. 6d). Note that the perturbation pressure field has a markedly 'four-cell' pattern at this time which is related to a transfer of mass from the cyclonic to the anticyclonic (anticyclonic to the cyclonic side) in the entrance (exit) region of the traveling momentum forcing associated with the meridional ageostrophic winds v'_a which exist in these regions (not shown). This mass adjustment causes a 'four-cell' pattern of vertical motion to be set up in the quadrants flanking the localized momentum forcing (Fig. 6c), with rising (sinking) motion in the northwest and southeast (southwest and northeast) quadrants.

By t = 48 h, the zonal counter current ($u' < 0$), portions of the meridional wind field, and the high-low p' dipole which were located in the exit region of the applied forcing are being advected downstream at the relative velocity U-c by the basic state flow (not shown), and are the PV anomaly generated by the external momentum forcing. The steady-state equilibrium (not shown) consists of a quasi-geostrophically balanced zonal jet streak with confluent (diffluent) flow in its entrance (exit) region, supported by a dipole couplet of low (high) perturbation pressure north (south) of the jet core. A dipole couplet of cold (warm) air whose center is colocated with the center of low (high) p' exists at all levels below the level of maximum zonal wind. This θ' field is reversed at levels above the jet core, whose horizontal gradients support the vertical shear of the zonal and meridional wind perturbations establishing thermal wind balance throughout the rotating Boussinesq atmosphere.

4. Conclusions

4.1 *Initial Value Problem*

- The initial PV anomaly governing the evolution in the geostrophic wind perturbations is given by the meridional gradient of the ageostrophic jet, $q'_i = -\partial u_{jet}/\partial y$.

• The initial zonal acceleration ($\partial u'_i/\partial t$) is due to the linear advection of the ageostrophic zonal jet by the basic flow ($-Du_{jet}/Dt$), and the initial meridional acceleration ($\partial v'_i/\partial t$) is associated with the Coriolis force acting on the unbalanced PV state.

• The steady-state equilibrium which conserves PV is a geostrophic zonal jet with meridionally confluent (diffluent) flow in its entrance (exit) region, supported by a dipole couplet of perturbation low (high) pressure north (south) of the jet core.

• Zonal counter currents ($u' < 0$) exist north and south of the main jet, and are portions of the perturbation return flow around the pressure couplet supporting the geostrophic jet.

• The geostrophic zonal jet is advected downstream by the basic state flow, establishing the physical mechanisms of geostrophic vorticity ($-\mathbf{U}\cdot\nabla\zeta'_g$) and horizontal temperature ($-\mathbf{U}\cdot\nabla\theta'$) advection.

• Linear theory predicts the preservation in both magnitude and geometry of a geostrophically *balanced* zonal jet streak introduced into both homogeneous and continuously stratified barotropic flows.

4.2 *Forced Problem*

• A PV anomaly is advected downstream at the relative velocity U-*c*, with steady-state geostrophic and ageostrophic circulations confined to the forcing region.

• For $t \leq \tau = 2a/(U-c)$, the zonal wind perturbation is similar in horizontal and vertical structure to the applied forcing since $\partial u'_i/\partial t = F\xi$. For $t > \tau$, the downstream advection of the PV anomaly generated by the external forcing dominates the perturbation response.

• For forcing geometry representative of the alongstream gradients of midlatitude jet streaks, the linear steady-state response is a zonally localized quasi-geostrophic (QG) jet streak.

• The external momentum forcing can either (i) enhance, (ii) destroy, or (iii) reinforce the PV associated with the initial disturbance.

4.3 *Effects of Nonlinearity*

• Theoretical analysis of the nonlinear QG field equations indicates that in a rotating Boussinesq flow, a four-cell pattern of vertical motion exists in the quadrants flanking the zonal jet core, consistent with that of real midlatitude jet streaks.

• Thermally direct (indirect) ageostrophic circulations exist in the entrance (exit) region at levels below the jet core, while thermally indirect (direct) circulations exist in the entrance (exit) region above the jet core which preserve the local thermal wind balance.

• In a rotating homogeneous atmosphere, the four-cell pattern of vertical motion is simply *reversed* from what occurs in a stratified atmosphere due to the constraints imposed by Taylor-Proudman mass continuity.

Part III. Publications To Date Resulting from the Research Project

Kaplan, M. L., S. E. Koch, Y.-L. Lin, R. P. Weglarz, and R. A. Rozumalski, 1994: The numerical simulation of meso-beta scale geostrophic adjustment processes resulting in secondary upper/lower-level jet formation and internal gravity waves during CCOPE. 6th AMS Conf. on Mesoscale Processes, 18-22 July, 1994, Portland, Oregon.

Weglarz, R. P., 1994: Three-dimensional geostrophic adjustment of homogeneous and continuously stratified atmospheres with application to the dynamics of midlatitude jet streaks. Ph. D. dissertation, Department of Marine, Earth, and Atmospheric Sciences, North Carolina State University, 389pp.

Weglarz, R. P., and Y.-L. Lin, 1994: Geostrophic adjustment and jetogenesis forced by impulsive and propagating zonal momentum sources in a rotating atmosphere. 6th AMS Conf. on Mesoscale Processes, 18-22 July, 1994, Portland, Oregon.

Part IV. Work in Progress and Work Objectives for the Period 06/94-11/94

(a) Two of the three 3D numerical simulations outlined in the November FY93 Semi-Annual Report have been completed. These are both coarse (16 km horizontal resolution) and nested (8 km horizontal resolution) grid simulations in which (i) the surface terrain of the inter-mountain region encompassing the western Great Plains and southwestern Canada has been replaced by a flat plateau of ~ 1500 m elevation with no horizontal terrain gradients, and (ii) the surface sensible heat flux is absent from a high resolution terrain run. Further analysis is currently in progress from the results of these simulations which will allow for a rigorous interpretation of the roles played by differential heating of the elevated terrain and associated radiative boundary layer processes in genesis of the simulated gravity wave episodes.

(b) The third of the three 3D numerical simulations outlined in the November FY93 Semi-Annual report which will address the role of moist thermodynamics, diabatic processes, and cloud microphysics on the amplitude, phase, and propagation speed of the simulated gravity waves as well as the formation of the observed Mesoscale Convective Complex (MCC) will be performed using the MESO, Inc. version of the MASS model.

(c) The first of two journal papers describing the synoptic and meso-α scale adiabatic geostrophic adjustment processes and the genesis of the first observed CCOPE

gravity wave event has been started, and it is expected to be submitted shortly to Monthly Weather Review for publication. A second journal article will be written and submitted to Monthly Weather Review which will focus on the role of terrain-induced circulations and diabatic processes and their effects on the geostrophic adjustment and genesis of the observed gravity waves, and will be started once analysis of the coarse and nested grid runs of the numerical simulation outlined in (b) above have been completed.

(d) Two journal articles describing the major conclusions of the theoretical work on geostrophic adjustment of homogeneous and continuously stratified flows with application to midlatitude jet streak dynamics which complements and supports the 3D numerical modeling studies have been started, and are planned to be submitted to the Journal of the Atmospheric Sciences. Tentative titles are: (i) Geostrophic Adjustment and Jetogenesis Forced by Impulsive and Propagating Zonal Momentum Sources. Part I: The Response of a Homogeneous Atmosphere of Finite Depth, and (ii) Geostrophic Adjustment and Jetogenesis Forced by Impulsive and Propagating Zonal Momentum Sources. Part II: The Response of Infinite and Semi-Infinite Continuously Stratified Atmospheres.

(e) A review article will be written which will focus on the major findings and applications of geostrophic adjustment theory that have taken place since Blumen's (1972) definitive study was published. This work will provide future researchers with a guide to previous work done on geostrophic adjustment in contemporary times (after 1972), and address the need for pursuing fundamental unanswered questions concerning this important dynamical process, much like present researchers who still refer to Blumen's work. Major conclusions found from the 3D numerical modeling and theoretical studies supported by this grant will also be included to show the importance of geostrophic adjustment processes in baroclinic severe storm producing environments.

References

Cahn, A., 1945: An investigation of the free oscillations of a simple current system. *J. Meteor.*, **2**, 113-119.

Kaplan, M. L., S. E. Koch, Y.-L. Lin, R. P. Weglarz, and R. A. Rozumalski, 1994a: The numerical simulation of meso-beta scale geostrophic adjustment processes resulting in secondary upper/lower-level jet formation and internal gravity waves during CCOPE. 6th AMS Conf. on Mesoscale Processes, 18-22 July, 1994, Portland, Oregon.

-------, R. A. Rozumalski, R. P. Weglarz, Y.-L. Lin, and S. E. Koch, 1994b: Numerical simulation studies of the role of convectively-driven ageostrophic jet streak adjustments in creating a favorable environment for the development of an isolated tornado outbreak. 6th AMS Conf. on Mesoscale Processes, 18-22 July, 1994, Portland, Oregon.

Koch, S. E., and R. E. Dorian, 1988: A mesoscale gravity wave event observed during CCOPE. Part III: Wave environment and probable source mechanisms. *Mon. Wea. Rev.*, **116,** 2571-2592.

Manobianco, J., S. E. Koch, V. M. Karyampudi, and A. J. Negri, 1994: The impact of assimilating satellite-derived precipitation rates on numerical simulations of the ERICA IOP 4 cyclone. *Mon. Wea. Rev.*, **122,** 341-365.

Rossby, C. G., 1938: On the mutual adjustment of pressure and velocity distributions in simple current systems, 2. *J. Mar. Res.*, **1**, 239-263.

Weglarz, R. P., 1994: Three-dimensional geostrophic adjustment of homogeneous and continuously stratified atmospheres with application to the dynamics of midlatitude jet streaks. Ph. D. dissertation, Department of Marine, Earth, and Atmospheric Sciences, North Carolina State University, 389pp.

Acknowledgments

This work was funded under NASA Contract #NAG 5-1790. The authors wish to acknowledge Dr. Ramesh Kakar for his support and Mr. David Hamilton for his work on the figures. The computer time was provided by the North Carolina Supercomputing Center. Dr. Ahmet Aksakal, formerly of NASA/GSFC, provided technical assistance with the use of the GMASS model.

List of Figures

Figure 1: GMASS simulation A (coarse grid, ~16 km horizontal resolution) of 500 mb wind vectors (alternate grid points plotted) and isotachs (ms^{-1}) valid at a) 0000 UTC, and b) 0600 UTC 11 July 1981.

Figure 2: GMASS simulation A of 500 mb height (solid in m) and temperature (dashed in C) valid at a) 0200 UTC and b) 0800 UTC, and c) 500 mb omega ($micbs^{-1}$) valid at 0500 UTC 11 July 1981. Indirect circulation cells denoted by "I".

Figure 3: GMASS simulation A of a) 500 mb wind vectors (plotted at alternate grid points) and isotachs (ms^{-1}) and b) 500 mb omega ($micbs^{-1}$) both valid at 1300 UTC 11 July 1981.

Figure 4: GMASS simulation B (nested grid, ~ 8 km horizontal resolution) of 500 mb omega ($micbs^{-1}$) valid at 1300 UTC 11 July 1982. Gravity wave troughs and ridges occur along nodal surfaces in the vertical motion field (denoted "T" and "R", respectively).

Figure 5: Linear theoretical response of an unbounded rotating Boussinesq atmosphere at t = 6h to the impulsive addition of localized zonal momentum.

Figure 6: Linear theoretical response of an unbounded rotating Boussinesq atmosphere at t = 12h as seen by a Galilean observer traveling at the speed $c < U$ due to a propagating zonal momentum forcing given by Eq. 14.

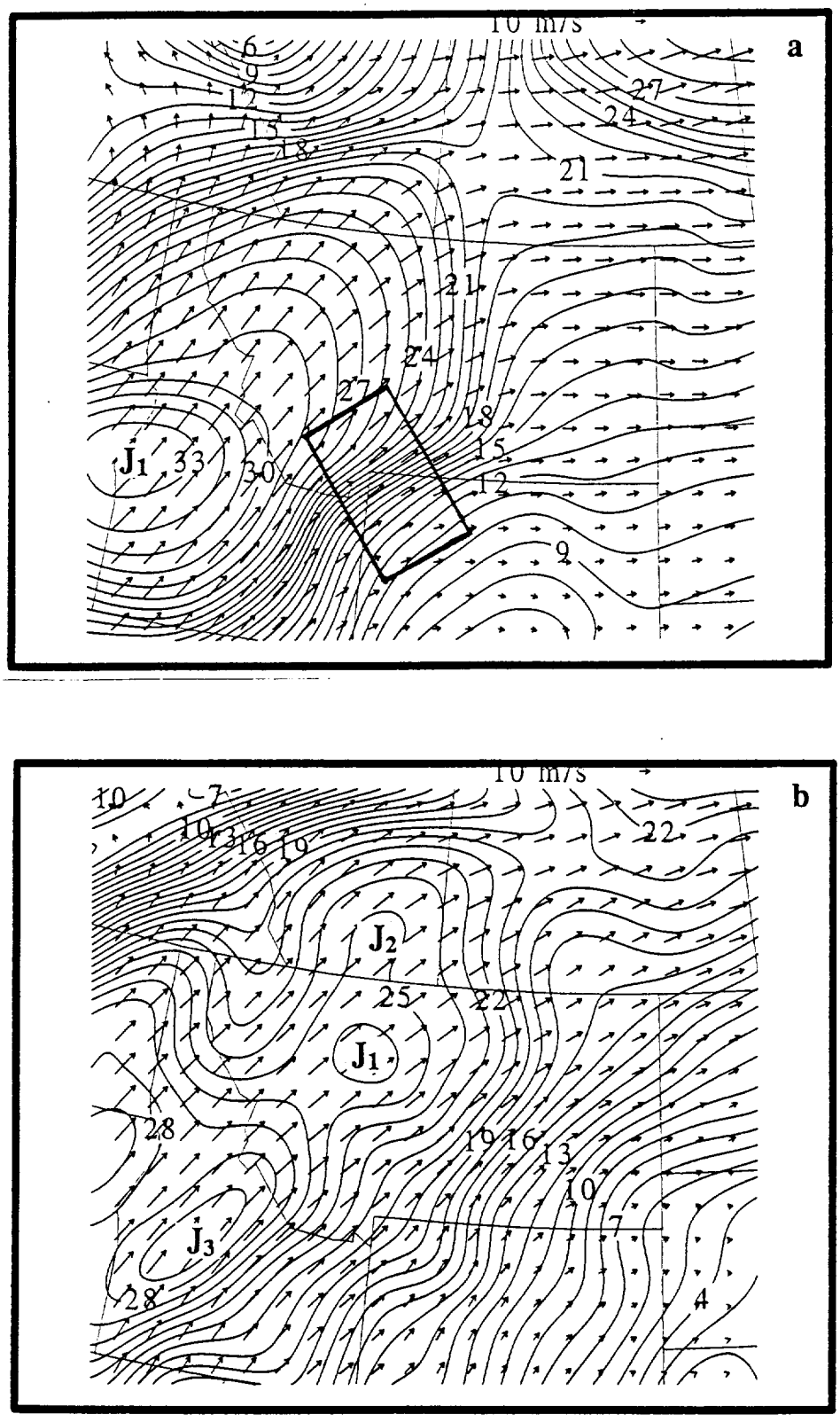

Figure 1

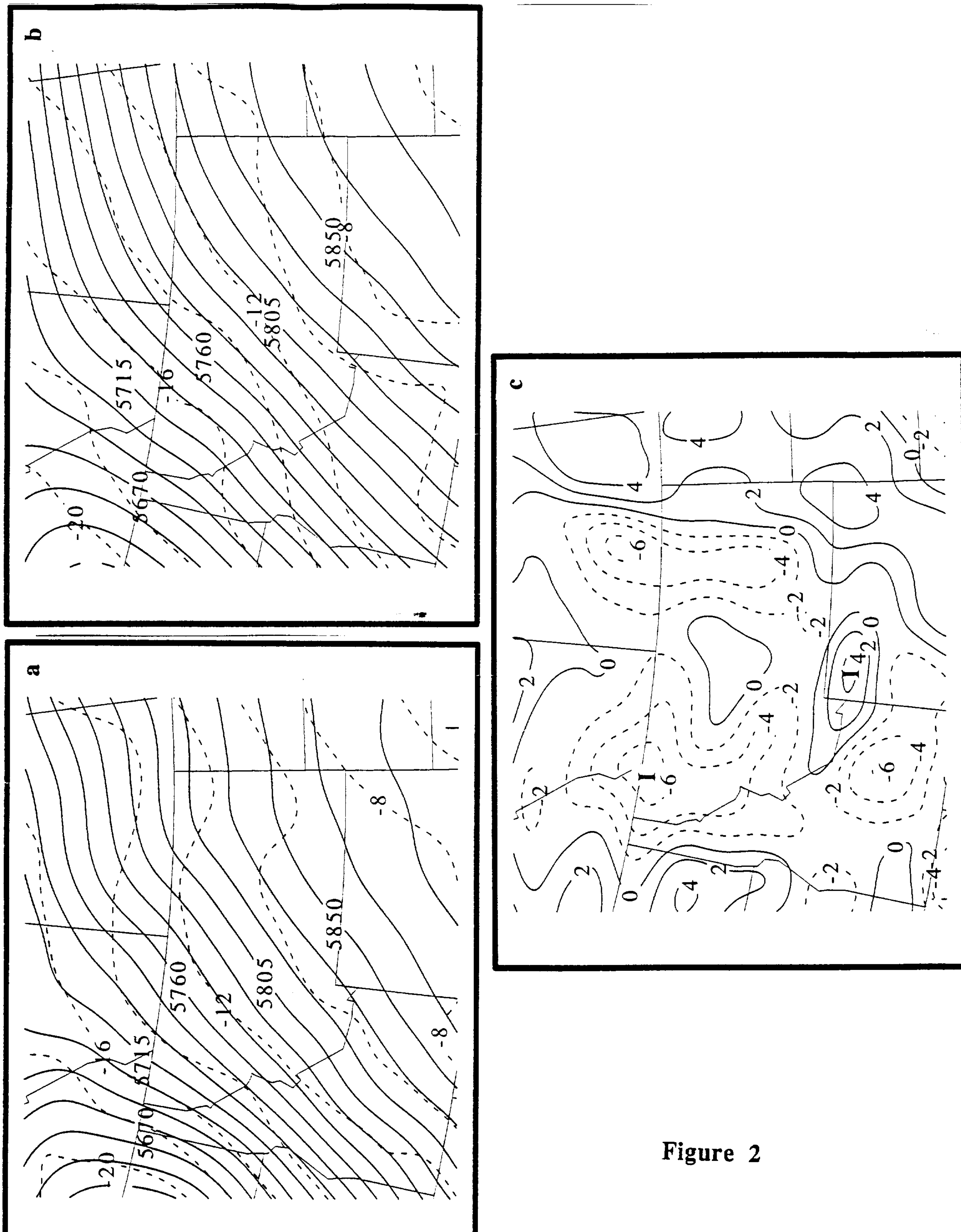
b
5715
5760
5805
5850
5670
-20
-16
-12
-8
a
5670
5715
5760
5805
5850
-20
-16
-12
-8
c
4
2
0
-2
-4
-6
I

Figure 2

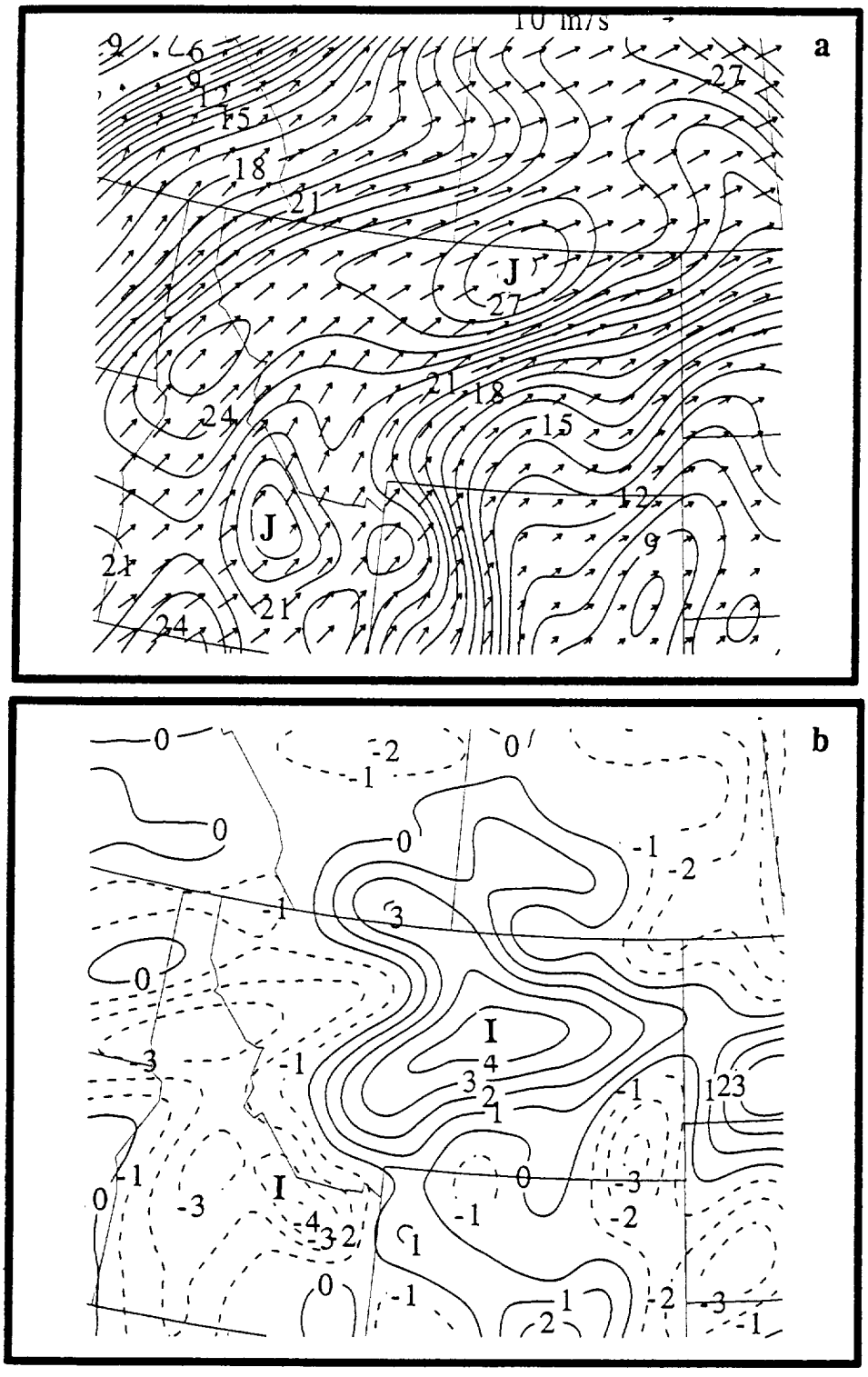

Figure 3

Figure 4

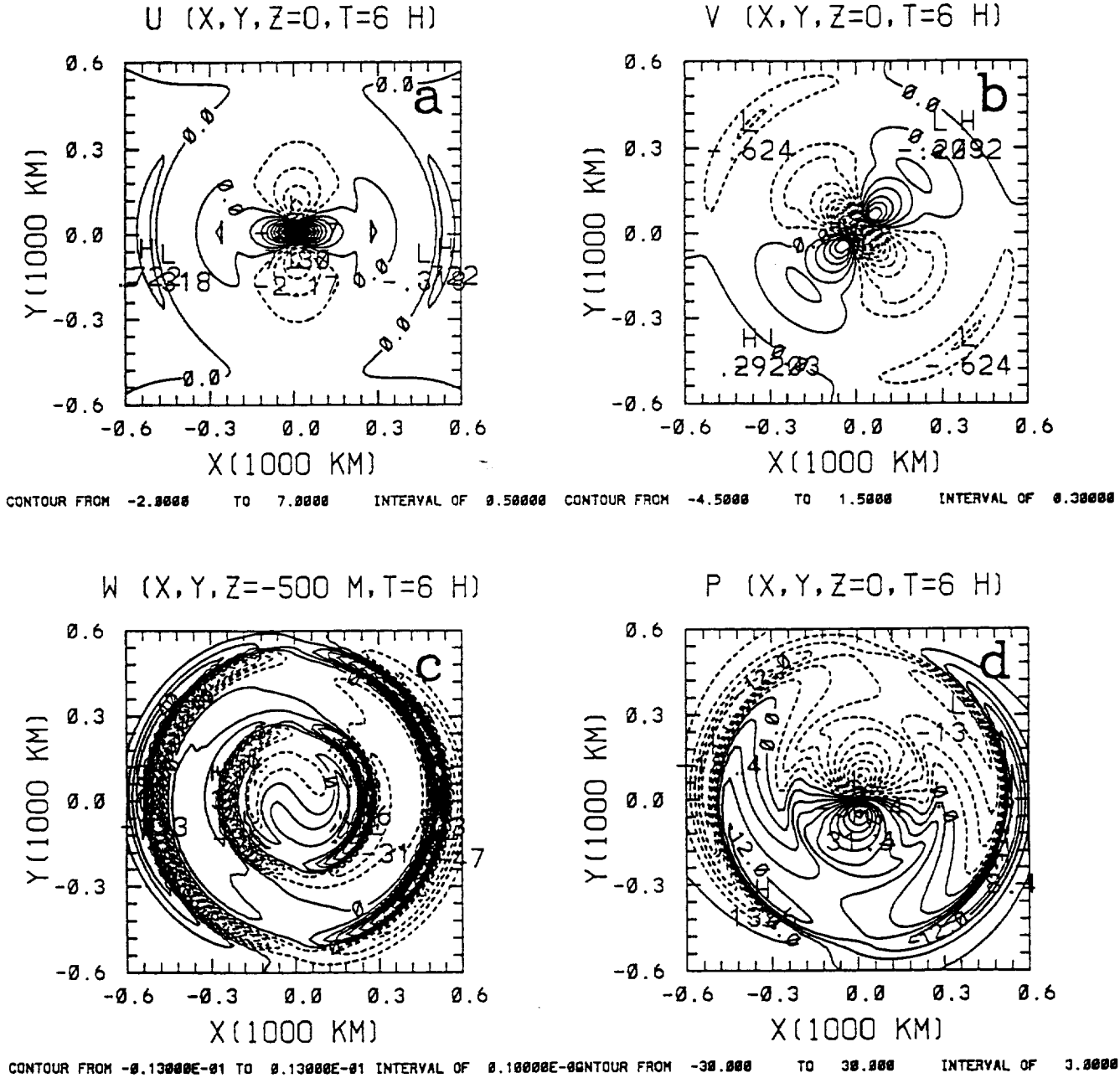
U (X, Y, Z=0, T=6 H)
V (X, Y, Z=0, T=6 H)
W (X, Y, Z=-500 M, T=6 H)
P (X, Y, Z=0, T=6 H)
a
b
c
d
Y(1000 KM)
X(1000 KM)
0.6
0.3
0.0
-0.3
-0.6
CONTOUR FROM -2.0000 TO 7.0000 INTERVAL OF 0.50000
CONTOUR FROM -4.5000 TO 1.5000 INTERVAL OF 0.30000
CONTOUR FROM -0.13000E-01 TO 0.13000E-01 INTERVAL OF 0.10000E-02
CONTOUR FROM -30.000 TO 30.000 INTERVAL OF 3.0000

Figure 5

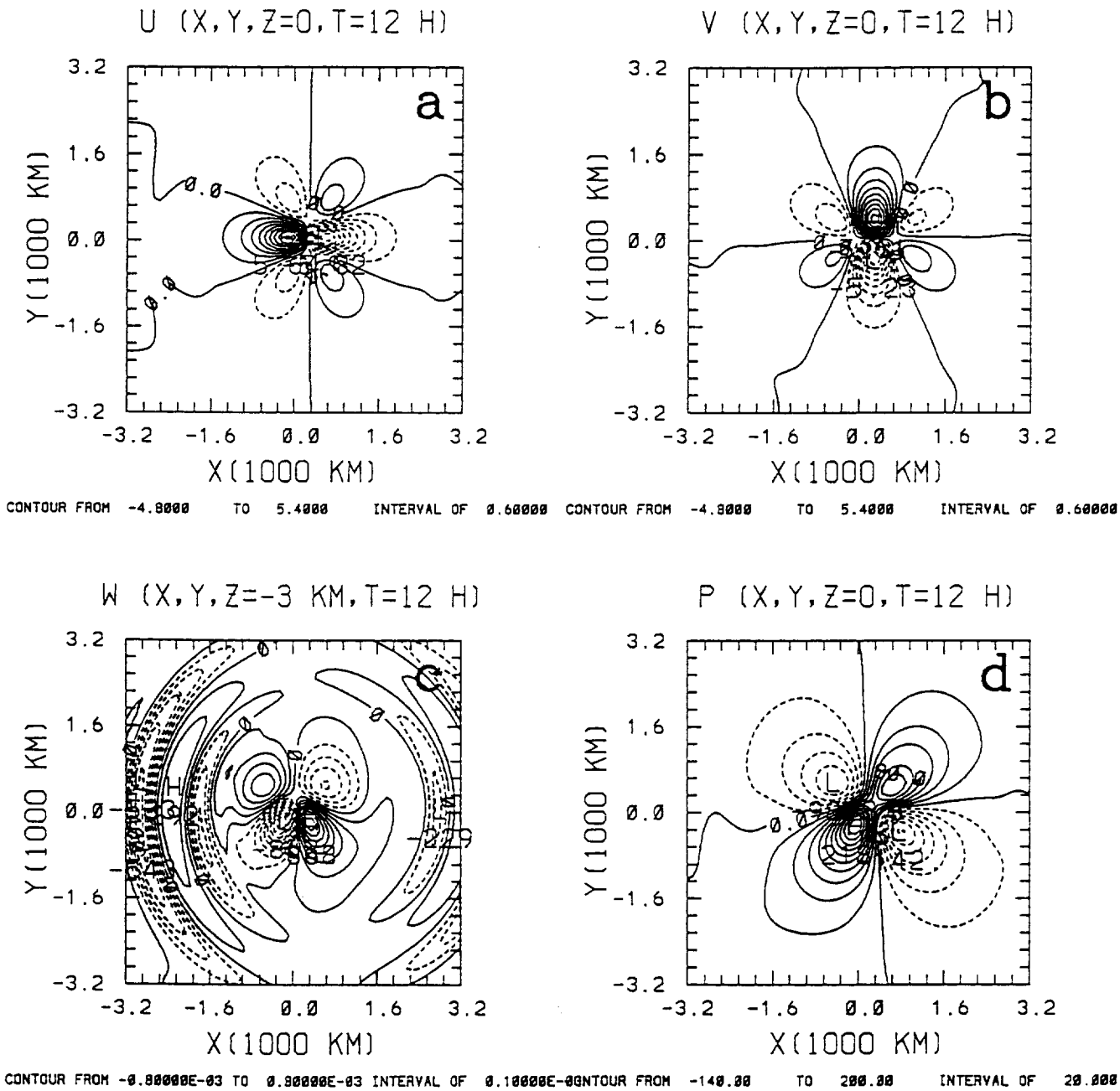
U (X,Y,Z=0,T=12 H)
V (X,Y,Z=0,T=12 H)
W (X,Y,Z=-3 KM,T=12 H)
P (X,Y,Z=0,T=12 H)
a
b
c
d
Y(1000 KM)
X(1000 KM)
3.2
1.6
0.0
-1.6
-3.2
CONTOUR FROM -4.8000 TO 5.4000 INTERVAL OF 0.60000
CONTOUR FROM -4.8000 TO 5.4000 INTERVAL OF 0.60000
CONTOUR FROM -0.80000E-03 TO 0.80000E-03 INTERVAL OF 0.10000E-03
CONTOUR FROM -140.00 TO 200.00 INTERVAL OF 20.000

Figure 6